Computational Materials Science II

Progress Report # 4

Vourvachakis S. Georgios
mse354

April 11, 2025

This work is licensed under a Creative Commons "Attribution-NonCommercial-NoDerivatives 4.0 International" license.

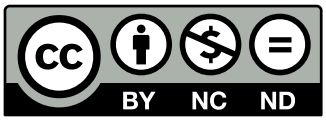

Contents

1

Introduction

The electronic and magnetic properties of crystalline materials are fundamentally determined by the way electrons interact with the periodic potential of a lattice. Density functional theory (DFT) has become the workhorse method for the theoretical determination of these properties. At its core, DFT transforms the many-electron problem into a tractable single-particle framework by solving the Kohn–Sham equations [1] under a self-consistent field scheme. When combined with techniques such as Brillouin zone sampling[2] and spin-polarized calculations[3], DFT can provide detailed insights into the band structure, density of states, and magnetic behavior of materials [4], [5].

1.1 Electronic Band Structure Calculations with DFT

In the DFT formalism, the electronic structure problem is formulated via the *Kohn–Sham equations*[6],[1]:[1]

$$\left[-\frac{\hbar^2}{2m}\nabla^2 + V_{\text{eff}}(\mathbf{r})\right] = \epsilon_{n\mathbf{k}}\psi_{n\mathbf{k}}(\mathbf{r}) \,,$$

where $\psi_{n\mathbf{k}}$ are the Bloch functions, $\epsilon_{n\mathbf{k}}$ are the Kohn–Sham eigenvalues, and V_{eff} is the effective potential that includes the external potential, the Hartree term, and the exchange-correlation potential. Owing to the periodicity of the crystalline lattice, Bloch's theorem applies:

$$\psi_{n\mathbf{k}}(\mathbf{r}) = e^{i\mathbf{k}\cdot\mathbf{r}} u_{n\mathbf{k}}(\mathbf{r}) \,,$$

where $u_{n\mathbf{k}}$ inherits the periodicity of the direct lattice.

1.2 Brillouin Zone Sampling and High-Symmetry Points

For periodic systems, the band energies $\epsilon_{n\mathbf{k}}$ are functions of the wave vector $\mathbf{k}$ within the first Brillouin zone (BZ). Rigorous determination of the band structure requires careful sampling of the BZ. In practice, one often chooses a set of *high-symmetry points* along which the band dispersions are computed. For instance, in an FCC (face-centred cubic) lattice the standard band path may be described by points such as

$$\Gamma \to X \to W \to K \to \Gamma \to L \to U \to W \to L \to K \to U \to X \,,$$

which capture the key features of the dispersion relations (see Brillouin zone sampling and Band structure in ASE website's stable version instance).

[1] For a more thorough analysis of the *variational optimization framework* under the Hohenberg-Kohn theorems and Kohn-Sham equations, refer to assignment 1.

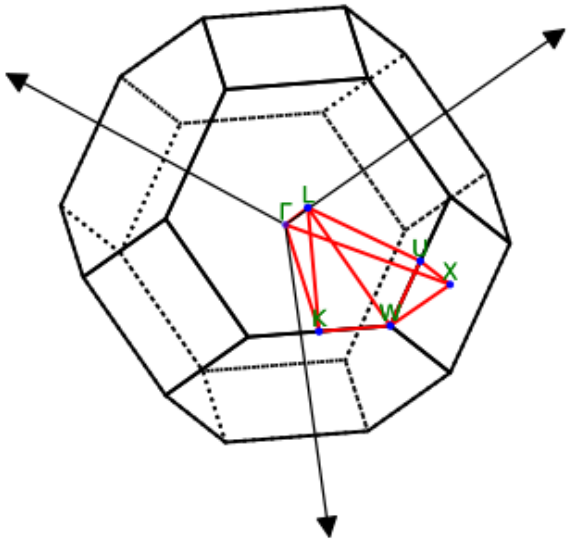

Figure 1: The image depicts the first Brillouin zone of a FCC lattice, shown as a truncated octahedron. Green markers indicate high-symmetry points in reciprocal space, connected by red lines that represent the standardized path for electronic band structure calculations. Solid lines show visible edges of the polyhedron, while dashed lines represent hidden edges. This representation from Setyawan and Curtarolo (2010) [7] illustrates the conventional path through momentum space used for consistent band structure analysis.

In practice, one constructs a sampling mesh in the BZ and then identifies the high-symmetry points. The eigenvalue problem is solved along paths connecting these points. In addition, corrections such as *spin-orbit coupling* may alter these band dispersions, which requires further adjustments in both the Hamiltonian and the k-space sampling (see Calculation of electronic band structures on GPAW tutorials).

The precision of the band structure calculation depends on how well the integration over the BZ is approximated. One defines the integrated quantity such as the total energy as

$$E_{\text{tot}} \coloneqq \sum_n \int_{\text{BZ}} f(\epsilon_{n\mathbf{k}}) \epsilon_{n\mathbf{k}} d\mathbf{k} \,,$$

where $f(\epsilon_{n\mathbf{k}})$ is the occupation function. Accurate integration techniques (e.g., using the Monkhorst–Pack scheme which can be further optimized invoking *generalized regular (GR) grids*[8][2]) involve both a dense mesh for total energy calculations and a refined path along high-symmetry directions for band dispersions.

[2] "On the fly" means that the algorithm does not require prior pre-calculation of GR grids stored in a database for a specific k-point density or crystal symmetry. Instead, when a user submits a DFT calculation with a specified real-space lattice, atomic positions, and desired k-point density, the algorithm rapidly searches through candidate GR grids (that preserve the lattice symmetry) and selects the optimal grid during the job execution. I cite this article here based on a recent discussion (on April 9, 2025) we had with prof. Kopidakis.

1.3 Density of States (DOS)

The (total) density of states $\rho(E)$ is a measure of the *number of electronic states per unit energy per unit volume*. It is defined as

$$\rho(E) \coloneqq \sum_n \int_{\mathrm{BZ}} \delta(E - \epsilon_{n\mathbf{k}}) d\mathbf{k} \Rightarrow \rho(E;\mathbf{k}) \overset{\text{gpaw}}{=} \sum_n \delta(E - \epsilon_{n\mathbf{k}}) \langle \psi_{n\mathbf{k}} | \psi_{n\mathbf{k}} \rangle \ ,$$

while the *projected density of states (PDOS)* projects $\rho(E)$ onto specific atomic orbitals or molecular states.[3]

At certain critical points in the BZ—where the derivative of the energy with respect to k vanishes—the DOS exhibits singularities known as *Van Hove singularities (VHSs)*[9]. For instance, if the dispersion is nearly flat near a critical point, the group velocity $\mathbf{v}_g^n \coloneqq \nabla_{\mathbf{k}} \epsilon_{n\mathbf{k}}$ becomes small, leading to a divergence (often logarithmic in 2D and as a step in 3D) in the DOS. These singularities have practical implications in phenomena like superconductivity[10] and enhanced electron correlation[11].

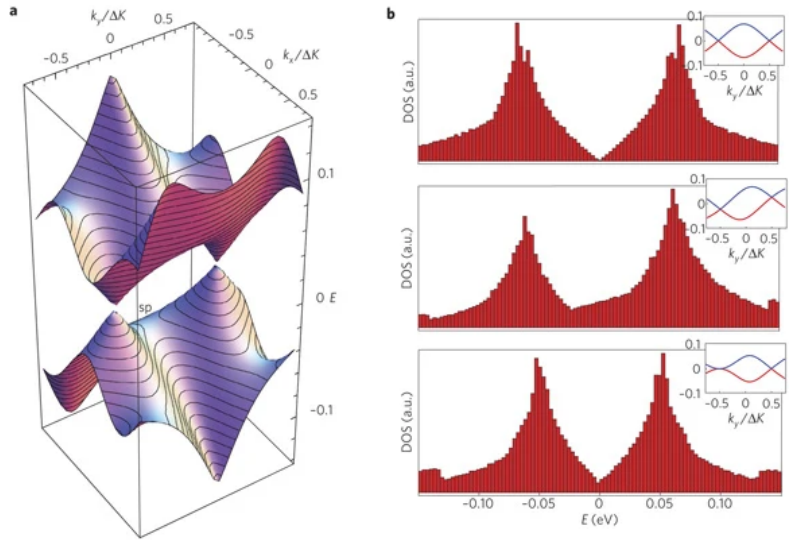

Figure 2: (a) Dispersion of lowest energy states for $\theta = 1.79°$, $t_\perp \approx 0.27$ eV, in a bilayer. A saddle point (marked 'sp') is visible between the two Dirac points in the negative energy band; another one exists in the positive energy band. (b) Top: DOS of a bilayer with VHSs corresponding to the energy of the saddle points for $\theta = 1.79°$, $t_\perp \approx 0.24$ eV and no interlayer bias; middle: same with interlayer bias $V_{\text{bias}} = 0.15$ V; bottom: same for a trilayer and no bias. Insets: The band energies along a line joining the two Dirac points for the corresponding layer configurations.[12]

1.4 Conduction vs. Insulation and Band-gap Considerations

From DOS plots, one can infer whether a material is metallic or insulating. A finite DOS at the Fermi level E_F signifies a conductor, whereas a gap (i.e., a region with $\rho(E) \approx 0$) indicates an insulator or semiconductor.

[3] The notation $\overset{\text{gpaw}}{=}$ associates a quantity (DOS in our case) to the convention of GPAW.

Although in an ideal calculation one expects the band-gap deduced from the band structure to match that from the DOS, in practice discrepancies may arise due to *broadening effects* (used to mimic temperature and instrumental resolution) and numerical integration errors. For further detail on DOS analysis, see Density of states in GPAW tutorials.

1.5 Electron Spin and Magnetic Structure: Spin-Polarized Calculations

In magnetic materials, the explicit treatment of electron spin becomes necessary. In *spin-polarized DFT*[3], the electron density is divided into contributions from spin-up ($n_\uparrow(\mathbf{r})$) and spin-down ($n_\downarrow(\mathbf{r})$) electrons:

$$n(\mathbf{r}) = n_\uparrow(\mathbf{r}) + n_\downarrow(\mathbf{r}) \,,$$
$$m(\mathbf{r}) = n_\uparrow(\mathbf{r}) - n_\downarrow(\mathbf{r}) \,,$$

where $m(\mathbf{r})$ represents the local magnetization[5]. The Kohn–Sham equations are then solved for both spin channels with an effective potential that includes spin-dependent exchange-correlation effects.

Hund's rule (the *maximum spin multiplicity principle*) states that electrons will occupy degenerate orbitals with parallel spins to maximize the total spin, thereby lowering the energy through exchange interaction[13]. For an isolated Fe atom (which nominally has a $[\mathrm{Ar}]3d^6 4s^2$ configuration), the application of Hund's rule yields a high-spin configuration. Schematically:

- **Spin-Up States:** The lower-energy d-orbitals are filled with electrons aligned in the same direction.
- **Spin-Down States:** The remaining electrons occupy higher energy states or, when symmetry and exchange energies are considered, lead to a net magnetic moment.

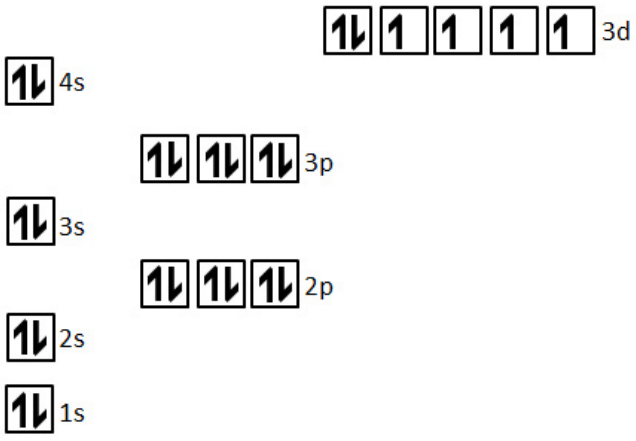

Figure 3: Hund's rule of maximum spin multiplicity for Fe atom. A comprehensive ground state electronic configuration diagram is given in webelements.

For example, if the majority spin (spin-up) levels are substantially populated compared to the minority (spin-down) levels, the difference in populations directly provides the net magnetic moment. Quantitatively,

one may write:

$$\mu = \mu_B (N_\uparrow - N_\downarrow) \,,$$

where $\mu_B \approx 5.7883817982 \times 10^{-5}$ eV/T is the Bohr magneton and $N_\uparrow$, $N_\downarrow$ are the numbers of spin-up and spin-down electrons, respectively. For a ground-state Fe atom, specifically, we have $\mu/\mu_B = 4$. However, due to the *delocalization of electron density* and *band formation*, in bulk BCC Fe we obtain $\mu/\mu_B \approx 2.22$ [13].

1.6 Magnetic Orderings

Based on the theoretical framework presented in Chapter 5 – Magnetics by Ozerov and Vorobyev[5], one may consider:

1. **Non-Magnetic Calculations:** In non-magnetic DFT, $n_\uparrow(\mathbf{r}) = n_\downarrow(\mathbf{r})$ and no net magnetic moment is present. This approximation is suitable when exchange-correlation effects do not lead to spontaneous symmetry breaking.
2. **Ferromagnetic Calculations:** In the ferromagnetic state, all the atomic moments align in the same direction. The self-consistent field (SCF) procedure is modified to allow for different potentials for spin-up and spin-down electrons, leading to $m(\mathbf{r}) \neq 0$ over the sample.
3. **Antiferromagnetic Calculations:** Here, neighboring atomic moments are antiparallel. In the SCF loop, a doubling (or more) of the unit cell is often required to capture the spin alternation. The net magnetic moment per cell may be zero even though local moments are large.

In spin-polarized (or magnetic) DFT calculations, the electron density is split into two parts (or *channels*) corresponding to electrons with "spin up" and "spin down". This division is necessary because electrons are spin-1/2 particles and can have one of two spin orientations. In practical terms:

- **Spin-up channel:** Contains all electrons with one (i.e., "up") spin orientation.
- **Spin-down channel:** Contains all electrons with the opposite (i.e., "down") orientation.

Each spin channel is treated separately in the SCF process, meaning that the Kohn–Sham orbitals (or bands) and the resulting DOS are computed independently for up and down electrons. The imbalance between the number of electrons in these channels directly gives the net magnetization, which we will later estimate numerically.

In a model of maximal polarization for an Fe atom, the spin-up channel occupancy per atom has 6 electrons. This means that, assuming the $3d$ electrons are arranged to favor parallel spin, five orbitals will each receive one electron with spin up, and the 6^{th} electron also goes in with spin up (or it may be understood that before pairing, one ideally would have more electrons in the *majority* spin channel, and thus $4s^{\uparrow}3d^{5*(\uparrow)}$ giving six spin-up unpaired valence electrons).

Spin-down channel occupancy per atom has 2 electrons. This comes from the fact that electrons that must pair (to obey the Pauli exclusion principle) contribute to the *minority* (spin-down) channel (or $4s^{\downarrow}3d^{\downarrow}$ such that $4s^{\downarrow}3d^{\downarrow} \star 4s^{\uparrow}3d^{5*(\uparrow)} \equiv 4s^{\uparrow\downarrow}3d^{(\uparrow\downarrow)+4*(\uparrow)} = 4s^{2}3d^{6}$, where "$\star$" denotes the convolution operator). The figure below illustrates an example of spin-up and spin-down channels for a case study on ferromagnetic semiconductor, EuO [14].

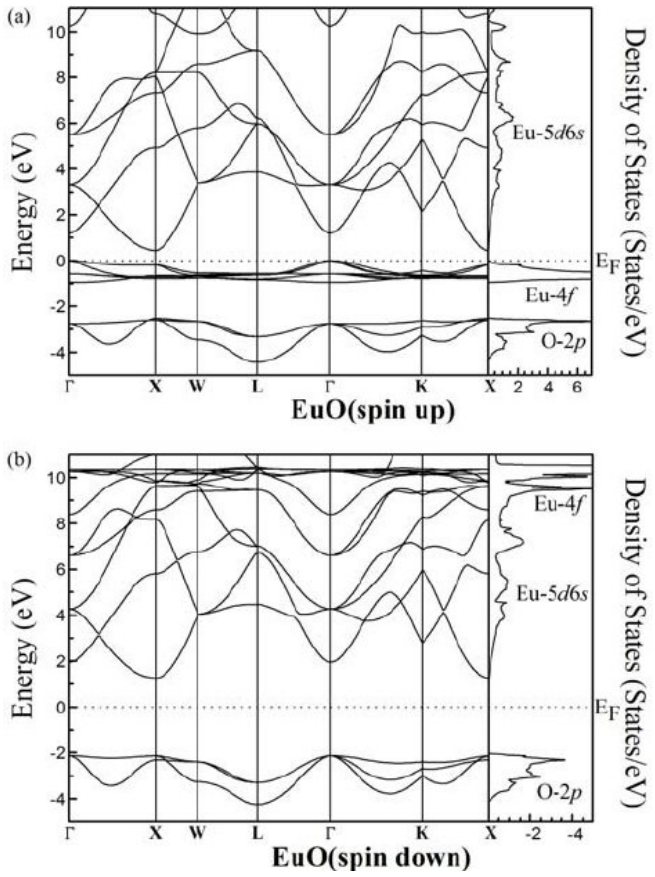

Figure 4: (a) Spin-up and (b) spin-down band structure (left panel) and corresponding density of states (right panel) of unstrained EuO in the ferromagnetic configuration with optimized bulk lattice parameters, a = 5.184 Å. The zero of energy is at the Fermi level, E_F.[14]

A rigorous treatment of spin-polarized DFT in the context of magnetism is provided in "Spin-Polarized DFT Calculations and Magnetism" by Rudolf Zeller (2006)[3]. In this work, the author emphasizes the role of the exchange-correlation potential in splitting the Kohn–Sham eigenvalues for different spin channels, and how this splitting determines the overall magnetic ordering.

The spin-dependent effective potential V_{eff}^{σ} (with $\sigma \in \{\uparrow, \downarrow\}$) is given by:

$$V_{\text{eff}}^{\sigma}(\mathbf{r}) = V_{\text{ext}}(\mathbf{r}) + V_{\text{HF}}(\mathbf{r}) + V_{\text{XC}}^{\sigma}[n_{\uparrow}(\mathbf{r}), n_{\downarrow}(\mathbf{r})] \, .$$

The solution of these equations then yields spin-resolved band structures and DOS, which are central to

understanding the magnetic behavior in crystalline materials (see Magnetic properties and Electron spin and magnetic structure on GPAW tutorials).

2 Results and Remarks

In this section of our work, we focus on calculating and analyzing the band structures of aluminum (Al) and silicon (Si) using DFT with the projector augmented-wave code GPAW. We adopt experimental lattice constants of $a = 4.05$Å for Al (fcc structure) and $a = 5.43$Å for Si (diamond structure). The aim is to determine whether Al and Si are conductors or insulators by examining the presence (or absence) of a band gap and calculate the Fermi level (E_F) for each material and compare with expected values from the literature. Subsequently, we perform DOS calculations for Si and Al, identifying how the DOS can confirm or contradict conclusions drawn from the band structure. Then, address spin-polarized or spin-orbit coupling (SOC) calculations as needed.

2.1 Electronic Band Structure of Aluminum and Silicon

Aluminum (Al): We select the fcc structure and set the lattice constant $a = 4.05$Å. Aluminum has a single atom in its primitive cell (magnetic moments initialized a 1×3 zero matrix).
Silicon (Si): We assign the diamond structure with a lattice constant $a = 5.43$Å. The diamond lattice contains two atoms per primitive cell (magnetic moments initialized a 2×3 zero matrix).

For regular (no spin-orbit coupling (SOC)) calculations, we use the PBE (Perdew–Burke–Ernzerhof) functional, a popular GGA (generalized gradient approximation) exchange-correlation functional.

For SOC calculations, we switch to LDA (local density approximation) in this example, as it is often used in the literature[4] for simpler test calculations with spin-orbit coupling.

An $8 \times 8 \times 8$ k-point mesh is selected for the ground-state calculation. For the band structure, we follow the high-symmetry path typically denoted for an fcc lattice or diamond structure. Specifically, the path `'GXWKGLUWLK'` is used (fig.5), which covers common high-symmetry directions in the Brillouin zone.

A plane-wave cutoff (`PW(400)`) of 400 eV is chosen to adequately converge the wavefunctions.

The electronic occupations are treated with a small Fermi–Dirac smearing of 0.01 eV, aiding convergence in metallic or near-metallic systems.

In the code implementation, `nbands_value` determines how many Kohn–Sham bands are included in

[4] Specifically, LDA+U first implemented by Shick et al. (1999) [15] seems to be the most prominent for SOC integration (e.g., [16]). In short, this functional incorporates Hubbard U parameters for certain orbitals at certain atoms. The magnetic moments and band eigenvalues obtained are in very good quantitative agreement with previous full-potential linear muffin-tin orbital calculations [15].

the calculation. For Al (metal), fewer bands might suffice if SOC is enabled (to avoid code constraints related to the local-orbital basis). For Si (semiconductor), more unoccupied bands (16, 20, or more) may be required for accurate conduction band details. `convergence='bands':conv_bands` ensures that at least a certain number of bands above the Fermi level are fully converged in the self-consistent loop.

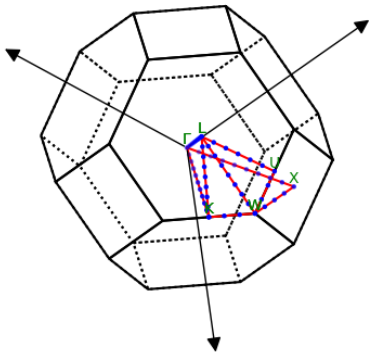

Figure 5: Band path (unit cell, path specification, special points, and interpolated k-points) of both FCC Al and Diamond Si, created indirectly using the `cell.bandpath()` method from GPAW, after performing the standard ground state calculation.

The table below provides a clear comparison between the electronic structure properties of silicon and aluminum, both with and without spin-orbit coupling (SOC). The notation VBM → CBM refers to the transition from valence band maximum to conduction band minimum. Aluminum is a conductor (metal). There is no band gap as clearly shown in both the numerical results and band structure diagrams (fig.6). The bands cross the Fermi level ($E = 0$ eV in the diagrams), which is characteristic of metallic behavior. This is consistent in both non-SOC and SOC calculations.

Silicon is a semiconductor (insulator at 0 K). Band gap (indirect):

- Non-SOC (PBE): 0.580 eV
- SOC (LDA): 0.464 eV

The band structure diagrams clearly show separation between valence and conduction bands (fig.7). The diagram indicates the calculated indirect gap is 0.053 eV, with experimental value of 1.120 eV (note: DFT calculations typically underestimate band gaps. See the analysis by J. Perdew (1986) [17] on the *Density functional theory and the band gap problem*).

The Fermi level (E_F) is the chemical potential of electrons in a solid at thermodynamic equilibrium[6]. It represents the energy level at which the probability of electron occupancy is exactly 0.5 at non-zero tem-

perature ($T > 0$ K). At absolute zero ($T = 0$K), the Fermi level marks the boundary between occupied and unoccupied electronic states. In band structure diagrams, the Fermi level is conventionally set to $E = 0eV$ ("grounded"). For the FCC Al we report the results below:

- Non-SOC (PBE): 7.2165 eV (Reference energy (E_{ref}) = −6603.423265 eV)
- SOC (LDA): 7.0168 eV (E_{ref} = −6578.421307 eV)

and for diamond Si:

- Non-SOC (PBE): 5.7327 eV (E_{ref} = −15772.688500 eV)
- SOC (LDA): 5.4493 eV (E_{ref} = −15717.426366 eV)

These Fermi level values represent the absolute energy position of the Fermi level with respect to a reference energy (often vacuum level but in not in our calculations). In the band structure diagrams, the Fermi level is normalized to 0 eV for visualization purposes.

Table 1: Ground State Properties for Silicon and Aluminum (PBE for Non-Soc, LDA for SOC)

Property	**Silicon**		**Aluminum**	
	Non-SOC	**SOC**	**Non-SOC**	**SOC**
Indirect Gap (eV)	0.580	0.464	None	None
Indirect Transition	$\Gamma \rightarrow X$ ($s = 0, k = 0, n = 3$) $\rightarrow$ ($s = 0, k = 8, n = 4$)	$\Gamma \rightarrow X$ ($s = 0, k = 0, n = 7$) $\rightarrow$ ($s = 0, k = 8, n = 8$)	N/A	N/A
Direct Gap (eV)	2.558	2.488	None	None
Direct Transition at	Γ point	Γ point	N/A	N/A
Different Direct/Indirect	Yes	Yes	No	No
Fermi Level (eV)	5.7327	5.4493	7.2165	7.0168

Table 2: Initialization Parameters for Silicon and Aluminum Calculations

Parameter	**Non-SOC**	**SOC**
xc	PBE	LDA
k-points	(8, 8, 8) mesh with Γ point	
Mode	pw with ecut = 400.0 eV	
Occupations	fermi-dirac, width = 0.01 eV, fixmagmom = False	
Symmetry	off	
SOC	False	True
magmoms	None	Si: [[0. 0. 0.][0. 0. 0.]] Al: [[0. 0. 0.]]
System Changes	positions, numbers, cell, pbc, initial_charges, initial_magmoms	

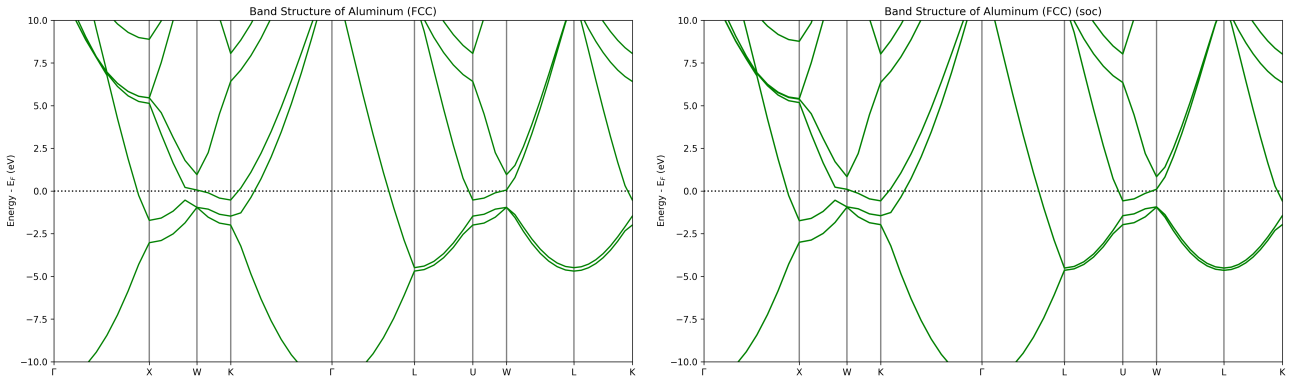

Figure 6: Band Structure of Aluminum (FCC). Comparison of Non-SOC (left) vs. SOC (right) Calculations. The band structure diagrams show electronic energy levels vs. k-path along high symmetry points ($\Gamma - X - W - K - \Gamma - L - U - W - L - K$) in the Brillouin zone (BZ). The dotted horizontal line at $E = 0$ eV represents the Fermi level. With the SOC effect introduced we notice a slight decrease in the VB-CB distance across L to K points.

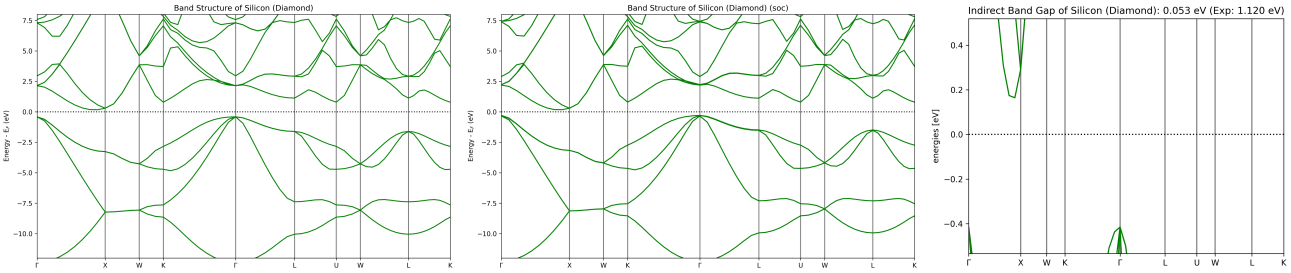

Figure 7: Electronic Structure of Silicon (Diamond). Band Structure without SOC (left), with SOC (center), and Detailed View of Indirect Band Gap (right). The band structure diagrams show electronic energy levels vs. k-path along high symmetry points in the BZ. The right panel highlights the indirect band gap of 0.053 eV compared to experimental value of 1.120 eV. The SOC induces spontaneous time-reversal symmetry breaking (due to the presence of magnetic order) evident in the Γ point (e.g., the figure on the Effect of spin-orbit coupling in GPAW tutorials).

2.2 DOS Inference

In DOS calculations, especially those handled by GPAW's DOSCalculator class, the purpose of broadening is to replace the idealized *delta peaks* (which would represent exact eigenvalue states) with smooth functions that give a more continuous density-of-states (DOS) spectrum. The routine in `dos.py` module does this by convolving the eigenvalues with a Gaussian function. The width parameter controls the width (standard deviation, σ) of this Gaussian. With a width of 0.1 eV, each eigenvalue is spread out over an energy range on the order of 0.1 eV, leading to a smoother DOS curve that is easier to interpret, while reducing the impact of any *numerical noise* or *discretization effects*.

Conductors (metals) have a non-zero DOS at the Fermi level ($\epsilon - \epsilon_F = 0$) and exhibit continuous distribution of states across the Fermi level. Aluminum's DOS clearly shows states present at the Fermi level, confirming its metallic nature (fig.8).

Insulators/semiconductors show a gap in the DOS around the Fermi level (a region where DOS ≈ 0). Silicon's DOS shows a distinct region near 0 eV where the DOS approaches zero, indicating a band gap.

The band gaps extracted from DOS and BS calculations may differ slightly due to broadening effects in DOS calculations, since they can artificially reduce the apparent band gap in DOS compared to BS. Moreover, DOS requires integration over the BZ, which depends on k-point sampling density, while band structures typically show only specific high-symmetry paths through k-space.

For Aluminum, both DOS and band structure consistently show no gap, confirming metallic behavior. The continuous distribution of states across the Fermi level in both analyses confirms its conductive nature.

For Silicon, the gap appears to be approximately $0.5 - 1.0$ eV (estimating from fig.9). The DOS-derived gap appears roughly consistent with the band structure calculations (0.580 eV (Non-SOC) and 0.464 eV (SOC)).

This analysis demonstrates how DOS plots complement band structure calculations, providing convergent evidence about the electronic nature and band gap characteristics of materials.

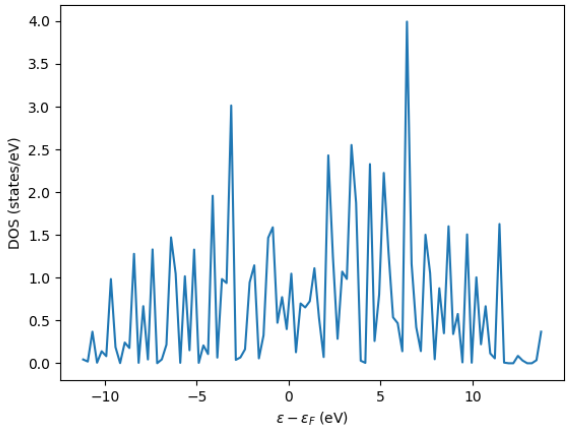

Figure 8: Density of States (DOS) for Aluminum (FCC). The DOS plot shows the distribution of electronic states as a function of energy relative to the Fermi level ($\epsilon - \epsilon_F$). Note the continuous non-zero DOS at the Fermi level (0 eV), characteristic of metallic behavior.

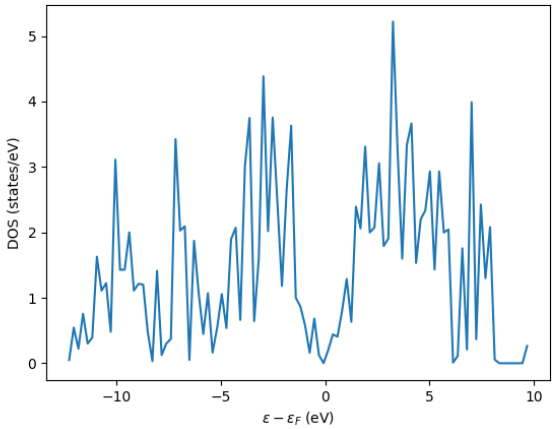

Figure 9: Density of States (DOS) for Silicon (Diamond Structure). The DOS plot shows the distribution of electronic states as a function of energy relative to the Fermi level ($\epsilon - \epsilon_F$). Note the region of near-zero DOS around the Fermi level, indicating a band gap characteristic of semiconductor behavior.

2.3 Spin Polarized Calculations on α-Fe

The electronic configuration of Fe is given as: $[Ar]3d^6 4s^2$, which contributes 8 valence electrons per atom. Hund's maximum multiplicity rule notes that—in order to minimize electron repulsion and maximize exchange energy—electrons will occupy different orbitals with parallel spins.

We discussed the Hund's rule or the *maximum spin multiplicity principle* and we sketched the spin occupation or one-Electron eigenvalue diagram for an isolated Fe atom (section 1.5, fig.3). The net contribution is: $\mu = gS\mu_B \approx 2 \times 2\mu_B = 4\mu_B$. Thus, the isolated Fe atom, when maximally polarized following Hund's rule, has a spin magnetic moment of approximately $4\mu_B$.

In the simulation, we study bulk Fe(bcc) or α-Fe in a two-atom unit cell. With 8 valence electrons per atom, the cell contains a total of 16 valence electrons.

Due to two factors—a different electron occupation in each spin channel (two-fold degeneracy) and the metallic nature of Fe—we must ensure that the basis of Kohn–Sham orbitals (the "bands") accommodates both the occupied states and a sufficient number of unoccupied states for the self-consistency at every k-point. In addition, for metals a common practice is to include at least 5 extra bands to allow for the k-point variations with fractional occupancy [18].

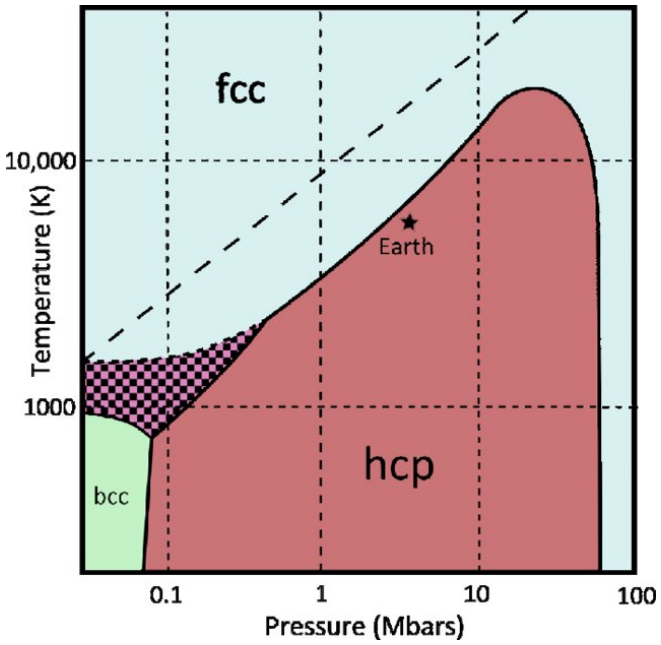

Figure 10: Phase diagram for iron at pressures and temperatures relevant to planetary heating. The HCP-FCC boundary has a very similar slope to that of a $T \propto P^{1/2}$ relationship (with the same slope as the dashed line shown). Since planetary heating would approximately track the HCP-FCC transition, it would be well-suited to the heating of a wide range of planetary masses $0.005 \sim 15 M_{\oplus}$ ("$\oplus$" is the planetary symbol of Earth). It is currently uncertain whether HCP can coexist with FCC Fe in the highlighted region. The highest temperature at which HCP iron can exist is $\sim 19,000$ K, corresponding to planets of a mass around $5 M_{\oplus}$.[19]

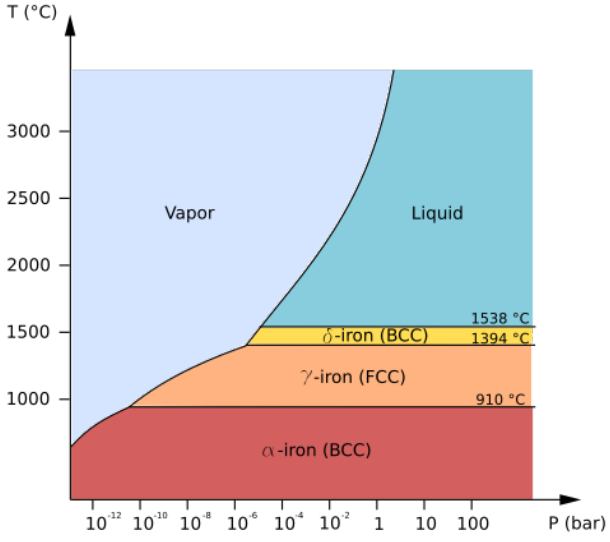

Figure 11: Low-pressure phase diagram of pure iron with its allotropes. Values taken from: William F. Smith, Scienza e tecnologia dei materiali (1995) (p. 241)[20]. We study the case of BCC Fe or α-Fe or ferrite. GPAW computes the ground state as a static 0K property at the given cell volume (and, by implication, zero external pressure) unless one explicitly sets up a finite-temperature or pressure-dependent calculation.

Assuming each Fe atom in isolation is maximally polarized, spin-up channel occupancy per atom has 6 electrons (from the maximally polarized $3d^6$ scheme) and spin-down channel occupancy per atom has 2 electrons (see subsection 1.6, where we now extend our discussion).

For a Two-Atom Unit Cell, assuming the ferromagnetic (FM) ordering (i.e., both atoms have their moments aligned in the same direction):

- **Majority (spin-up) in the FM state:** 6 electrons per atom × 2 atoms = 12 electrons.
- **Minority (spin-down) in the FM state:** 2 electrons per atom × 2 atoms = 4 electrons.

The net difference is $12 - 4 = 8$ electrons for the unit cell.[5]

Since the calculation is spin polarized, the number of bands chosen for each spin channel should be high enough to cover the highest filled (majority) channel. Thus, a minimal *number of bands per spin channel* is given by the number of electrons in that channel plus an extra 5 bands. In the FM case, one would choose:

$$\texttt{nbands} \geq 12 + 5 = 17 \text{ per spin degeneracy or channel .}$$

In practice, codes like VASP, GPAW, or Quantum ESPRESSO have a single parameter for `nbands` such that the same number of bands is used for both spin channels. Thus, to safely capture the majority channel occupancy plus extra metallic states, one might choose 17 or more bands in total (meaning 17 for each spin channel when spin polarization is active).

For nonmagnetic calculations, the 16 electrons are equally divided (8 per spin channel), so one would ideally have:

$$8 + 5 = 13 \text{ bands per spin degeneracy or channel .}$$

However, when comparing different magnetic phases (nonmagnetic, ferromagnetic, and antiferromagnetic), it is best to use a number that is safely large for all cases. Typically, one would choose `nbands` corresponding to the ferromagnetic case.

2.3.1 Initial Magnetic Moment Assessment

Since self-consistent field (SCF) calculations may converge to a local minimum that does not represent the desired magnetic order, it is essential to "seed" the calculation with reasonable initial magnetic moments (using parameters like `magmoms` in the `Atoms` constructor.

Here are sensible starting guesses for a two-atom unit cell:

- **Nonmagnetic Calculation:** Guess $0\mu_B$ for both atoms. In a nonspin-polarized calculation, the electrons are treated as paired with no net moment.

[5] Note that this is a simplified picture used to help understand Hund's rule in the atomic context. In the bulk solid, hybridization and bonding typically reduce the effective moment to around $2.2\mu_B$ per atom.

- **Ferromagnetic Calculation:** For each atom, set an initial moment near the experimental bulk value (which is about $2.22\mu_B$ per Fe atom). Although the isolated atom exhibits a $4\mu_B$ moment, the delocalization and bonding in the bulk reduce the moment to around $\sim 2.2\mu_B$[13].
- **Antiferromagnetic Calculation:** For the two atoms in the unit cell, specify opposite moments of similar magnitude. In an antiferromagnetic state, the system has local moments that are antiparallel; hence the total magnetization cancels while retaining a nonzero absolute local moment (the "absolute magnetization")[21].

These choices allow the SCF cycles to relax toward the true magnetic ground state for each phase, and the extra bands ensure that the calculation can capture the metallic behavior correctly.

In light of the above, we develop two separate modules with enhanced flexibility for parameter testing:

1. The first module (`ferro.py`) sets up and runs a spin-polarized DFT+U calculation for bcc Fe using GPAW and ASE for a given ordering (FM, Anti-FM, NM) and Hubbard U parameter. Command-line arguments allow efficient exploration of different magnetic configurations and U values without modifying the source code.
2. The second module (`magnetic_phases.py`) loads the saved calculations for the ferromagnetic, antiferromagnetic, and nonmagnetic phases to compare their energies (both LDA+U and the estimated PBE via an xc-difference correction) and to check the calculated magnetic moments.

Specifically, we first set up a two-atom unit cell (using a simple cubic lattice with a basis) with experimental lattice constant $a = 2.87$ Å, with the two atoms placed at fractional coordinates (0,0,0) (edge) and (0.5, 0.5, 0.5) (body). Each Fe atom is initialized with a magnetic moment of:[6]

- FM: (2.2, 2.2) (a.u.),
- Anti-FM: (-2.2,2.2) (a.u.),
- NM: (0,0) (a.u.),

with $2.2\mu_B$ being close to the experimental value for bulk bcc Fe. The calculation is performed using GPAW in plane-wave mode with a cutoff of 500 eV (increased from the original 350 eV for better accuracy) and a $10\times10\times10$ k-point sampling mesh (increased from the original $6\times6\times6$ mesh). Additionally, a Hubbard U correction is applied to the Fe d-orbitals, with the U value specified as a command-line parameter (default 1.0 eV).

The SCF result is then saved to a respective '`ordering_Uvalue.gpw`' file for downstream comparison, where '`ordering`' is one of '`ferro`', '`antiferro`', or '`non`', and '`value`' is the Hubbard U parameter used. Then, we load the pre-computed GPAW wavefunction files for the three magnetic states with the specified U value and compare their energies.

[6] The atomic unit of magnetic moment is the Bohr magneton, $\mu_B = 1\,a.u.$

We use the stored electron densities from LDA+U calculations along with the exchange-correlation (xc) energy difference to estimate the PBE (GGA) energies without re-running the SCF cycle. Finally, we compute the energy differences (with respect to the FM state) and the magnetic moments for the FM state.

The first table organizes the Hubbard analysis results by U value, showing the Fermi levels and converged energies for each magnetic configuration. The second table presents the energy differences between states and includes the magnetic moments data.

Table 3: Analysis of different Hubbard U values for BCC Fe

Parameter	**U = 0.5 eV**	**U = 1.0 eV**	**U = 1.5 eV**	**U = 2.0 eV**
Ferromagnetic				
Fermi level (eV)	9.11631	9.16632	9.25285	9.73032
Converged energy (eV)	-19.2009	-18.4585	-17.7606	-17.0924
Antiferromagnetic				
Fermi level (eV)	9.49608	9.63563	9.77071	9.34309
Converged energy (eV)	-18.2299	-17.3454	-16.5399	-15.6676
Non-magnetic				
Fermi level (eV)	9.18713	9.16371	9.14255	9.12522
Converged energy (eV)	-17.9439	-16.7932	-15.6466	-14.5064
Common parameters				
Reference energy: -69115.878741 eV				
Gap: None				
Direct/indirect transitions: No difference				
Input parameters: kpts = [10 10 10], mode = {ecut: 500.0, name: pw}, setups = {Fe: :d,U_{value}}				
System changes: positions, numbers, cell, pbc, initial_charges, initial_magmoms				
Hubbard parameters: l = 2, scale = True				

Table 4: Energy differences and magnetic moments for different U values

State	**U = 0.5 eV**		**U = 1.0 eV**		**U = 1.5 eV**		**U = 2.0 eV**	
	LDA+U	PBE	LDA+U	PBE	LDA+U	PBE	LDA+U	PBE
Ferro	0.000	0.000	0.000	0.000	0.000	0.000	0.000	0.000
Antiferro	0.971	0.928	1.113	0.943	1.221	1.021	1.425	0.825
Non-magnetic	1.257	1.147	1.665	1.097	2.114	1.051	2.586	0.987
Magnetic moments for ferromagnetic Fe (per atom): ($U = U_{\text{value}} : [\mu_1, \mu_2]$)								
U = 0.5 eV: [2.37718986 2.37713681]								
U = 1.0 eV: [2.59913103 2.59911705]								
U = 1.5 eV: [2.69605379 2.69608029]								
U = 2.0 eV: [2.78329332 2.78186542]								

In these results, the calculation with $U = 0.5$ eV yields a magnetic moment of $\sim 2.38 \mu_B$ per atom, which is closest to experiment. Even though the moment is still relatively high, the respective energy differences are smaller and the computed moment is in better agreement with experimental data.

Thus, for obtaining a DOS that properly reflects the correct exchange splitting and band formation yielding the experimental magnetic moment—the calculation performed with **U = 0.5 eV** should be used.

2.3.2 Estimating the Net Magnetic Moment from the DOS

In a spin-polarized calculation, the electrons are separated into two "spin channels" (spin-up and spin-down). Each channel has its own set of eigenvalues and contributes a separate DOS. The net magnetic moment is proportional to the difference between the number of electrons in the spin-up channel and that in the spin-down channel. In other words, if you integrate the DOS of each channel over the occupied energy range (up to the E_F), then the difference (multiplied by the Bohr magneton) gives the net magnetic moment. GPAW (and other DFT codes) computes the net moment internally, but we can verify it by performing the integration on the DOS.

Thus we include an extended version of the DOS plotting routine (in `plot_dos.py`, used in the previous analysis (section 2.2)) that (in addition to plotting) numerically integrates (trapezoidal rule) the DOS for each spin channel and computes the net number of electrons difference. (If the DOS is given in units of states/eV, then the integration over energy gives the total number of states.) For a spin-polarized calculation, the net spin polarization (in electrons) is

$$\Delta N = \int_{-\infty}^{\epsilon_F} \mathrm{DOS}_{\uparrow}(\epsilon)d\epsilon - \int_{-\infty}^{\epsilon_F} \mathrm{DOS}_{\downarrow}(\epsilon)d\epsilon \equiv \Delta m \ (a.u.) \,,$$

similar with the "channel separation" of electron density (eq.1.5) and net magnetization description (eq.1.5) in subsection 1.5.

The results of the numerical integration are summarized in the following table.

Magnetic Ordering	Ferromagnetic	Antiferromagnetic	Non-magnetic
Spin-up electrons	10.076	6.837	–
Spin-down electrons	5.683	6.833	–
Net Magnetic Moment (μ_B per unit cell)	4.392	0.004	0

Table 5: Summary of integrated electron counts up to the Fermi level and net spin polarization for Fe under ferromagnetic, antiferromagnetic, and non-magnetic orderings.

In the ferromagnetic state, the DOS integration reveals an imbalance between the two spin channels. This results in a *net spin polarization* of 4.392 electrons and, hence, an estimated net magnetic moment of 4.392 μ_B per unit cell. Such a significant spin imbalance is consistent with the presence of a substantial magnetic moment in ferromagnetic Fe.

Conversely, in the antiferromagnetic ordering, nearly identical integrated electron counts for the two channels yield an almost zero net spin polarization (0.004 electrons), which corresponds to a negligible net

magnetic moment. This is expected because, in antiferromagnets, *local moments are aligned antiparallel*, effectively canceling each other.

For the non-magnetic state, a non-spin-polarized calculation inherently provides a single DOS without any spin splitting; thus the net magnetic moment is 0. These observations align well with experimental findings where bulk Fe exhibits a measurable magnetic moment in its ferromagnetic phase, while antiferromagnetic and non-magnetic phases do not show an overall magnetization.

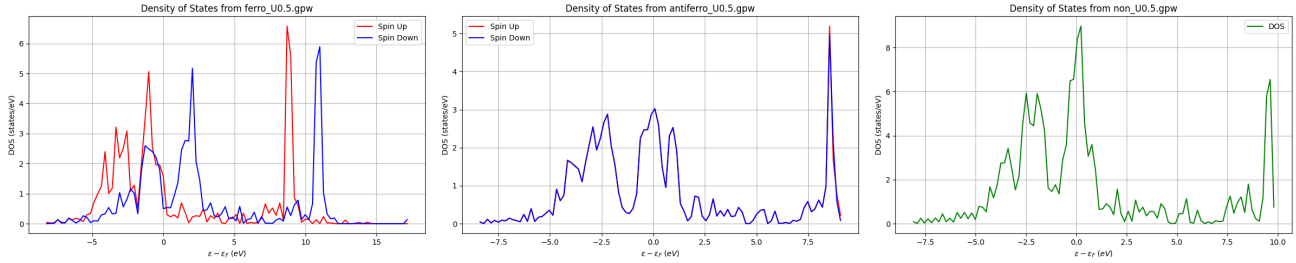

Figure 12: Spin-Resolved (left, middle) and Nonspin-Polarized (right) DOS for BCC Fe at $U = 0.5$ eV with default gaussian broadening of $\sigma = 0.01$ eV (default). Left: Ferromagnetic Fe exhibits distinct spin-up (red) and spin-down (blue) DOS, indicating a net magnetic moment ($\approx 2.38 \mu_B$ per atom) close to the experimental value of $2.2 \mu_B$ [13],[22]. Center: The antiferromagnetic DOS likewise shows two spin channels, but these offset each other in total occupancy, yielding no net magnetic moment. Right: A nonmagnetic DOS (single green curve) has degenerate spin channels and thus zero net moment. The clear spin imbalance in the ferromagnetic DOS (left panel), along with the near-experimental magnetic moment, confirms that $U = 0.5$ eV reproduces known observations of bulk Fe's magnetic and electronic structure [23].

3

Environment Setup

This reference guide specifies user-dependent components of Python codes for performing Density Functional Theory (DFT) calculations using the GPAW (Grid-based Projector Augmented Wave method) software package and ASE (Atomic Simulation Environment).

The codes are organized in the directory `HW_4_codes` after `tag.gz` compression. The sub-directories address various computational results including plots, `gpw`, `json`, and `txt` files (in `HW_4_codes/prior_runs/`). `HW_4_codes/results_bs/` directory contains the files of the band structure calculation (the DOS was plotted using the `plot_dos.py` module from GPAW's gitlab repository) and . In general, one can reproduce and verify the validity of the experiments across the report, given the appropriate resources for manageable execution time and version GPAW $\geq$ 25.1.0, and play around with alternative more accurate setups discussed in the respective sections.

The workflow for the bulk BCC Fe magnetic structure analysis follows a *stateful computational pipeline*, in order to generate the appropriate `gpw` files for downstream processing:

`ferro.py` → `magnetic_phases.py` or/and `ferro.py` → `plot_dos.py`.
Execution must adhere to the defined topological order to ensure input consistency and validity across stages.

Remark 3.1. All modules require a proper GPAW (and thus ASE) environment setup. Before running any calculation, users must modify the path settings to match their local installation.

The following function is imported in all scripts of the aforementioned sub-directories and requires user-specific modifications:

```
def setup_gpaw_paths(): # routine for gpaw setting
    # Suppress detailed GPAW output
    os.environ['GPAW_VERBOSE'] = 'o'
    sys.stdout = open(os.devnull, 'w')  # Redirect standard output

    # Clear existing paths and set the new one [user-dependent]
    intended_path = os.path.expanduser("~/Desktop/DFT_codes/gpaw_datasets"
    "/gpaw-setups-0.9.20000")
    setup_paths[:] = [intended_path]  # Replace all existing paths
    os.environ['GPAW_SETUP_PATH'] = intended_path

    sys.stdout = sys.__stdout__  # Restore standard output
    print("GPAW looking for datasets in:", setup_paths)
    print("Environment GPAW_SETUP_PATH:", os.environ['GPAW_SETUP_PATH'])
```

3.1 Adjusting the Path Settings

Users must update the `intended_path` variable to match their local GPAW dataset installation:

1. Locate your GPAW setups directory (typically installed with GPAW or downloaded separately).
2. Replace `'~/Desktop/DFT_codes/gpaw_datasets/gpaw-setups-0.9.20000'` with the path to your setups directory.
3. Ensure the path format is appropriate for your operating system:
   - Linux/macOS: Use `'/path/to/gpaw-setups'` .
   - Windows: Use `'C:/path/to/gpaw-setups'` or `r'C:\path\to\gpaw-setups'` .

References

[1] W. Kohn and L. J. Sham. "Self-Consistent Equations Including Exchange and Correlation Effects". In: *Phys. Rev.* 140 (4A Nov. 1965), A1133–A1138. DOI: 10.1103/PhysRev.140.A1133. URL: https://link.aps.org/doi/10.1103/PhysRev.140.A1133.

[2] Shunsuke A Sato. "Two-step Brillouin zone sampling for efficient computation of electron dynamics in solids". In: *Journal of Physics: Condensed Matter* 34.9 (Dec. 2021), p. 095903. ISSN: 1361-648X. DOI: 10.1088/1361-648x/ac3f00. URL: http://dx.doi.org/10.1088/1361-648X/ac3f00.

[3] Rudolf Zeller. "Spin-Polarized DFT Calculations and Magnetism". In: *John von Neumann Institute for Computing* (2006). URL: https://api.semanticscholar.org/CorpusID:18497686.

[4] Fatima et al. "Chapter One - Electronic structure and density functional theory". In: *Fundamentals of Multiscale Modeling of Structural Materials*. Ed. by Wenjie Xia and Luis Alberto Ruiz Pestana. Elsevier, 2023, pp. 3–35. ISBN: 978-0-12-823021-3. DOI: https://doi.org/10.1016/B978-0-12-823021-3.00007-5. URL: https://www.sciencedirect.com/science/article/pii/B9780128230213000075.

[5] Ruslan P. Ozerov and Anatoli A. Vorobyev. "5 - Magnetics". In: *Physics for Chemists*. Ed. by Ruslan P. Ozerov and Anatoli A. Vorobyev. Amsterdam: Elsevier, 2007, pp. 305–360. ISBN: 978-0-444-52830-8. DOI: https://doi.org/10.1016/B978-044452830-8/50007-6. URL: https://www.sciencedirect.com/science/article/pii/B9780444528308500076.

[6] D.S. Sholl and J.A. Steckel. *Density Functional Theory: A Practical Introduction*. Wiley, 2011. ISBN: 9781118211045. URL: https://books.google.gr/books?id=_f994dmAdv0C.

[7] Wahyu Setyawan and Stefano Curtarolo. "High-throughput electronic band structure calculations: Challenges and tools". In: *Computational Materials Science* 49.2 (2010), pp. 299–312. ISSN: 0927-0256. DOI: https://doi.org/10.1016/j.commatsci.2010.05.010. URL: https://www.sciencedirect.com/science/article/pii/S0927025610002697.

[8] Wiley S. Morgan et al. "Generalized regular k-point grid generation on the fly". In: *Computational Materials Science* (2019). URL: https://api.semanticscholar.org/CorpusID:119329929.

[9] Wenbin Wu et al. "The discovery of three-dimensional Van Hove singularity". In: *Nature Communications* 15 (Mar. 2024). DOI: 10.1038/s41467-024-46626-9.

[10] Hyeok-Jun Yang and Yi-Ting Hsu. "Optical absorption signatures of superconductors driven by Van Hove singularities". In: *Phys. Rev. B* 111 (5 Feb. 2025), p. 054514. DOI: 10.1103/PhysRevB.111.054514. URL: https://link.aps.org/doi/10.1103/PhysRevB.111.054514.

[11] Hyeong Jun Lee, Choong H. Kim, and Ara Go. "Hund's metallicity enhanced by a van Hove singularity in cubic perovskite systems". In: *Phys. Rev. B* 104 (16 Oct. 2021), p. 165138. DOI: 10.1103/PhysRevB.104.165138. URL: https://link.aps.org/doi/10.1103/PhysRevB.104.165138.

[12] Guohong Li et al. "Observation of Van Hove singularities in twisted graphene layers". In: *Nature Physics* 6.2 (Nov. 2009), pp. 109–113. ISSN: 1745-2481. DOI: 10.1038/nphys1463. URL: http://dx.doi.org/10.1038/nphys1463.

[13] Eleftherios N. Economou. "The Physics of Solids: Essentials and Beyond". In: 2010. URL: https://api.semanticscholar.org/CorpusID:93381551.

[14] Wen-Yi Tong et al. "Spin-dependent optical response of multiferroic EuO: First-principles DFT calculations". In: *Physical Review B* 89 (Jan. 2014). DOI: 10.1103/PhysRevB.89.064404.

[15] A. B. Shick, A. I. Liechtenstein, and W. E. Pickett. "Implementation of the LDA+U method using the full-potential linearized augmented plane-wave basis". In: *Phys. Rev. B* 60 (15 Oct. 1999), pp. 10763–10769. DOI: 10.1103/PhysRevB.60.10763. URL: https://link.aps.org/doi/10.1103/PhysRevB.60.10763.

[16] Hao Wang and Kenji Konashi. "LDA+U study of Pu and PuO2 on ground state with spin–orbital coupling". In: *Journal of Alloys and Compounds* 533 (2012), pp. 53–57. ISSN: 0925-8388. DOI: https://doi.org/10.1016/j.jallcom.2012.03.117. URL: https://www.sciencedirect.com/science/article/pii/S0925838812006421.

[17] John P. Perdew. "Density functional theory and the band gap problem". In: *International Journal of Quantum Chemistry* 28 (1986), pp. 497–523. URL: https://api.semanticscholar.org/CorpusID:97879042.

[18] Eric Cancès et al. "Numerical stability and efficiency of response property calculations in density functional theory". In: *Letters in Mathematical Physics* 113.1 (Feb. 2023). ISSN: 1573-0530. DOI: 10.1007/s11005-023-01645-3. URL: http://dx.doi.org/10.1007/s11005-023-01645-3.

[19] Robin Spivey. "Planetary Heating by Neutrinos: Long-Term Habitats for Aquatic Life if Dark Energy Decays Favourably". In: *Journal of Modern Physics* 4 (Dec. 2013), pp. 20–47. DOI: 10.4236/jmp.2013.412A1004.

[20] W.F. Smith et al. *Scienza e tecnologia dei materiali*. Collana di istruzione scientifica. Serie di ingegneria meccanica. McGraw-Hill Education, 2012. ISBN: 9788838667657. URL: https://books.google.gr/books?id=99TUMQEACAAJ.

[21] J. Stöhr and H. Siegmann. "From Fundamentals to Nanoscale Dynamics". In: *Magnetism: From Fundamentals to Nanoscale Dynamics, by J. Stöhr and H.C. Siegmann. Springer Series in Solid-State Physics, Vol. 152. Berlin: Springer, 2006.* 152 (Jan. 2006). DOI: 10.1007/978-3-540-30283-4.

[22] Victor L. Moruzzi, James Janak, and A. R. Williams. "Calculated electronic properties of metals". In: 1978. URL: https://api.semanticscholar.org/CorpusID:94453850.

[23] Jürgen Kübler. *Theory of Itinerant Electron Magnetism, 2nd Edition*. Oxford University Press, Sept. 2021. ISBN: 9780192895639. DOI: 10.1093/oso/9780192895639.001.0001.